Comparative Performance of a Thermal Barrier Coating System Utilizing Platinum Aluminide Bond Coat on Alloys CMSX-4® and MAR M® 002DS[1]

H. M. Tawancy

Luai M. Al-Hadhrami

Center for Engineering Research
and Center of Research Excellence
in Corrosion,
Research Institute,
King Fahd University of Petroleum
and Minerals,
P. O. Box 1639,
Dhahran 31261, Saudi Arabia

It is known that the relative performance of thermal barrier coatings is largely dependent upon the oxidation properties of the bond coat utilized in the system. Also, the oxidation properties of diffusion-type bond coats (aluminides and their modifications) are functions of the superalloy substrate used in blade applications. Therefore, the performance of a given coating system utilizing a diffusion-type bond coat can significantly vary from one superalloy to another. Toward the objective of developing coating systems with more universal applicability, it is essential to understand the mechanisms by which the superalloy substrate can influence the coating performance. In this study, we examined the relative performance of yttria-stabilized zirconia/platinum aluminide coating system on alloys CMSX-4 and MAR M 002DS representing single-crystal and directionally-solidified alloy systems respectively using thermal exposure tests at 1150 °C with a 24-h cycling period to room temperature. Changes in coating microstructure were characterized by various electron-optical techniques. Experiment showed that the coating system on alloy MAR M 002DS had outperformed that on alloy CMSX-4, which could be related to the high thermal stability of the bond coat on alloy MAR M 002DS. From a detailed microstructural characterization, this difference in behavior could be explained at least partially in terms of variation in chemical composition of the two alloys, which was also reflected on the exact failure mechanism of the coating system. [DOI: 10.1115/1.4004131]

1 Introduction

Application of thermal barrier coatings as surface protection systems for gas turbine blades allows the turbine entry temperature to be increased by as much as 200 °C leading to more power output, less fuel consumption, and cleaner environments, e.g., Ref. [1]. State-of-the-art technology involves the deposition of a of metallic bond coat (usually a modified aluminide-type) on the superalloy followed by a top coat of yttria-stabilized zirconia acting as a thermal insulator, e.g., Ref. [2]. The function of the bond coat is to develop an oxide layer acting as a "glue" to enhance the adhesion of the ceramic top coat, and provide an additional resistance to oxidation. However, one limitation of these coating systems is the dependence of the overall coating performance on the superalloy substrate composition. To develop coating systems of more universal applicability, it is important to develop an in-depth understanding of coating degradation modes as functions of superalloy substrate composition. In a recent study, we have shown that for a γ-γ' platinum bond, the Ti content of the superalloy substrate can have a significant effect on the coating performance [3].

It is the objective of this study to compare the performance of a thermal barrier coating system utilizing a platinum-aluminide bond coat deposited on commercial grades of the single-crystal alloy CMSX-4® and the directionally solidified alloy MAR M® 002. Emphasis has been placed upon: (i) microstructural features in the as-deposited condition, (ii) thermal stability, (iii) oxidation behavior, and failure mechanism.

2 Procedure

Table 1 shows the nominal chemical compositions of the alloys included in the study. All samples were in the form of rods about 10 cm in length and 8 mm in diameter. The bond coat with nominal Pt and Al contents of 55 and 25 wt. %, respectively, was applied by electroplating a 6–8 μm layer of Pt followed by an aluminizing treatment, and preoxidation/diffusion heat treatment at 1150 °C to develop the bond coat microstructure as well as a thin layer of aluminum oxide about 1 μm in thickness to enhance the adhesion of the ceramic top coat. In the as-deposited condition, the bond coat on both alloys had a nominal total thickness of about 55 μm including the interdiffusion zone. Subsequently, a layer of the ceramic top coat (zirconia +8 wt. % yttria) about 250 μm in thickness was deposited on the oxidized bond coat using the technique of electron-beam physical vapor deposition [4].

Thermal stability, oxidation behavior, and coating performance were determined from thermal exposure tests at 1150 °C in air with a 24-h cycling period to room temperature. Additional thermal exposure tests were carried out at 1000 and 1050 °C to study the kinetics of interdiffusion between the superalloy substrate and bond coat. Various techniques used to characterize the microstructure included scanning electron microscopy (SEM) combined with energy dispersive X-spectroscopy, electron probe microanalysis, transmission electron microscopy (TEM) and diffraction, and X-diffraction. Thin-foils for transmission electron microscopy were prepared by combination of electropolishing and ion beam thinning to observe the bond coat microstructure near the surface. All foils were examined at an accelerating voltage of 200 keV.

[1]®CMSX and MAR M are registered trademarks of Cannon-Muskegon and Martin Marietta Corporations, respectively.

Contributed by the International Gas Turbine Institute (IGTI) of ASME for publication in the Journal of Engineering for Gas Turbines and Power. Manuscript received April 11, 2011; final manuscript received April 12, 2011; published online October 28, 2011. Editor: Dilip R. Ballal.

Table 1 Nominal Chemical Compositions of Alloys CMSX-4® and MAR M® 002DS (wt. %)

Element	Ni	Co	Cr	Al	Ti	Mo	W	Ta	Hf	Re	Zr	Fe	C
Alloy CMSX-4®	Bal.	9.5	6.2	5.5	1	0.6	6.5	6.5	0.1	2.9	–	–	–
Alloy MAR M® 002DS	Bal.	10	9	5.5	1.5	0.5[a]	10	2.5	1.25	–	0.055	0.5[a]	0.15

[a]Maximum.

3 Results and Discussion

3.1 Microstructure in the As-Deposited Condition. Qualitatively, the coating microstructure on both alloys exhibited similar features in the as-deposited condition as illustrated in Fig. 1. Figures 1(*a*) and 1(*b*) show backscattered SEM composition images (Z-contrast images) along a cross-section of the coating and into the superalloy substrates. It is observed that for both alloys, the bond coat could be divided into three distinct layers: (i) an outer layer about 20 μm in thickness and exhibiting brighter

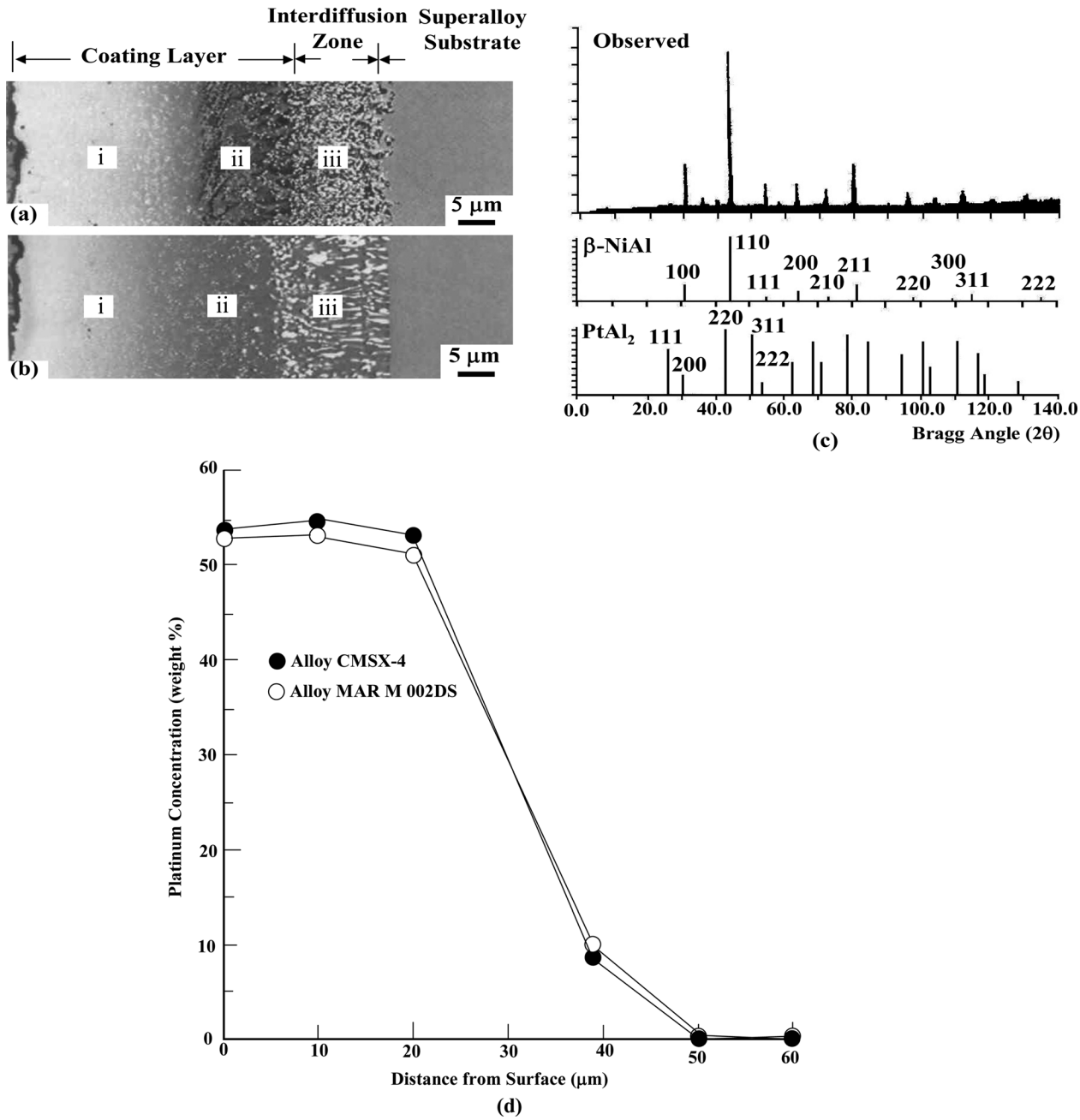

Fig. 1 Characteristic microstructural features in the as-deposited condition. (*a*) and (*b*) are backscattered SEM composition images along a cross-section of the bond coat and into alloys CMSX-4 and MAR M 002DS, respectively; the three bond coat layers i, ii, and iii are indicated. (*c*) X-ray diffraction pattern representative of the outermost layer of the Pt-aluminide bond coat on both alloys; standard patterns of β-NiAl and $PtAl_2$ are also shown. (*d*) Concentration profiles of Pt along a cross-section of the bond coat and into the substrates.

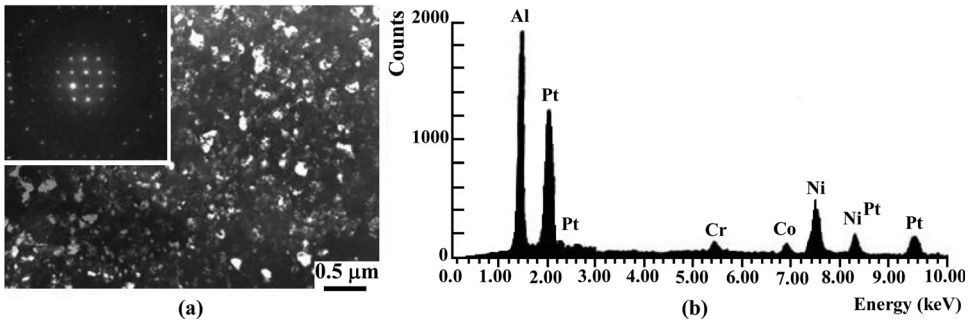

Fig. 2 An example derived from the bond coat on alloy CMSX-4 illustrating the microstructure of $PtAl_2$ in the outermost coating layer in the as-deposited condition. (*a*) Dark-field TEM image formed with the [200] reflection; the inset is a microdiffraction pattern in <001> orientation consistent with the structure of $PtAl_2$. (*b*) Corresponding energy dispersive X-spectrum illustrating the elemental composition of $PtAl_2$.

contrast indicating a higher average atomic number, (ii) an intermediate layer about 20 μm in thickness and exhibiting darker contrast corresponding to a lower average atomic number, and (iii) an inner interdiffusion zone about 15 μm in thickness. However, the interdiffusion zone of alloy CMSX-4 exhibited a finer structure in comparison with alloy MAR M 002DS, which could be related to differences in the chemical composition of the two alloys as described below. An X-diffraction pattern representative of outermost coating layer on both alloys is shown in Fig. 1(*c*). All diffraction lines were consistently indexed in terms of the structures of β-NiAl (cubic B2-type; $a = 0.2888$ nm) and $PtAl_2$ (Cubic, CaF_2-type; $a = 0.5930$ nm). Since Pt can replace for both Ni and Al [5], it is expected some Pt could also partition to the β-phase in the outermost coating layer. Consistent with these results, concentration profiles derived from microprobe analysis along cross-section of the bond coat and into the superalloy substrate showed that most of the Pt was concentrated within the outermost coating layer as shown in Fig. 1(*d*). As can be seen, similar results were obtained for both alloys. Therefore, the brighter contrast exhibited by the outermost coating layer on both alloys could be related to the higher Pt concentration (higher average atomic number).

Figure 2 is an example illustrating the microstructure of $PtAl_2$ as revealed by dark-field TEM imaging. It is observed that $PtAl_2$ was present as a fine dispersion (bright contrast) within the matrix of β-phase (dark contrast) as illustrated in Fig. 2(*a*). A microdiffraction pattern of the respective cubic structure of $PtAl_2$ in the <001> orientation is shown in the inset. The elemental composition of $PtAl_2$ is shown Fig. 2(*b*). Although some elements particularly Ni and Co could be present within particles of $PtAl_2$ in solid-solution replacing for Pt, it is also possible that a portion of these elements as well as Cr observed in the spectrum of Fig. 2(*b*) could have originated from the surrounding matrix.

Earlier studies of diffusion aluminide coatings such as the bond coat included in this study have shown that the kinetics of interdiffusion between the coating and superalloy substrate during thermal exposure at elevated temperatures are critically dependent upon the concentration of refractory elements in the superalloy as well as their distribution within the interdiffusion zone [6]. Although the nominal refractory element contents of alloys CMSX-4 and MAR M 002DS are about the same as shown in Table I, two compositional parameters could possibly lead to the difference in the microstructure of interdiffusion zone observed in Figs. 1 and 2: (i) the absence of C in alloy CMSX-4 and presence of Re and (ii) the presence of C in alloy MAR M 002DS and absence of Re as described below.

Figure 3 illustrates the results of analyzing the structure of the interdiffusion zone corresponding to alloy CMSX-4. A backscattered SEM composition image is shown in Fig. 3(*a*). An energy dispersive X-spectrum showing the elemental composition of the matrix phase is shown in Fig. 3(*b*). Quantitative microprobe analysis indicated that corresponding composition was consistent with that of γ'-phase with a nominal as shown in Fig. 3(*c*). It is to be noted that Re is known to have a stabilizing effect on the γ'-phase [7]. Detailed analysis of the precipitates observed within the interdiffusion zone indicated a base composition of Ni–Cr–W as demonstrated in the energy dispersive spectrum of Fig. 3(*d*). It is known that σ-phase exists over a wide range of composition in the Ni–Cr–W although it is not thermodynamically stable in any of the respective binary systems [8].

In contrast with the case of alloy CMSX-4, the composition of matrix phase of the interdiffusion zone corresponding to alloy MAR M 002DS was found to be more consistent with that of *b*-phase as shown in Figs. 4(*a*)–4(*c*). Because of the higher enthalpy of formation and binding energy of β-phase in comparison with γ'-phase [9], the interdiffusion zone corresponding to alloy MAR M 002DS is expected to have higher stability in comparison with the case of alloy CMSX-4 as confirmed by the results of thermal stability characteristics presented later. Also, the presence of C in alloy MAR M 002Ds can allow the interdiffusion zone to accommodate more refractory elements in the form of carbides as

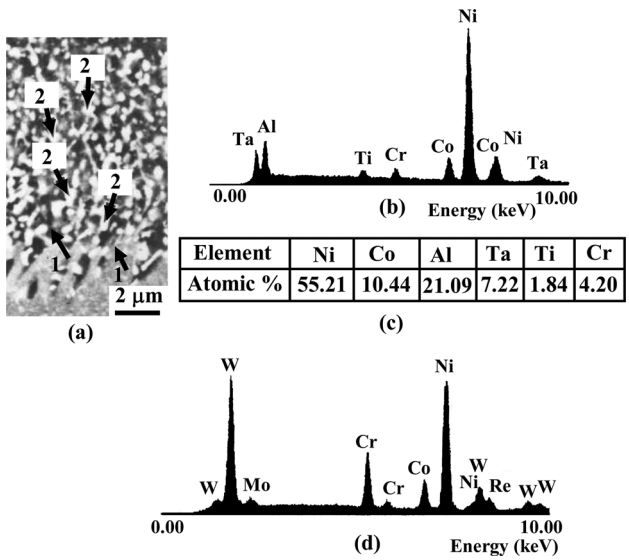

Element	Ni	Co	Al	Ta	Ti	Cr
Atomic %	55.21	10.44	21.09	7.22	1.84	4.20

(c)

Fig. 3 Analysis of the composition of interdiffusion zone of the coating on alloy CMSX-4 in the as-deposited condition. (*a*) Backscattered SEM composition image showing the microstructure of the interdiffusion zone. (*b*) Energy dispersive X-spectrum showing the elemental composition of the matrix phase (regions marked 1). (*c*) Composition of the matrix phase as determined by electron probe microanalysis. (*d*) Energy dispersive X-spectrum representative of the precipitates (regions marked 2).

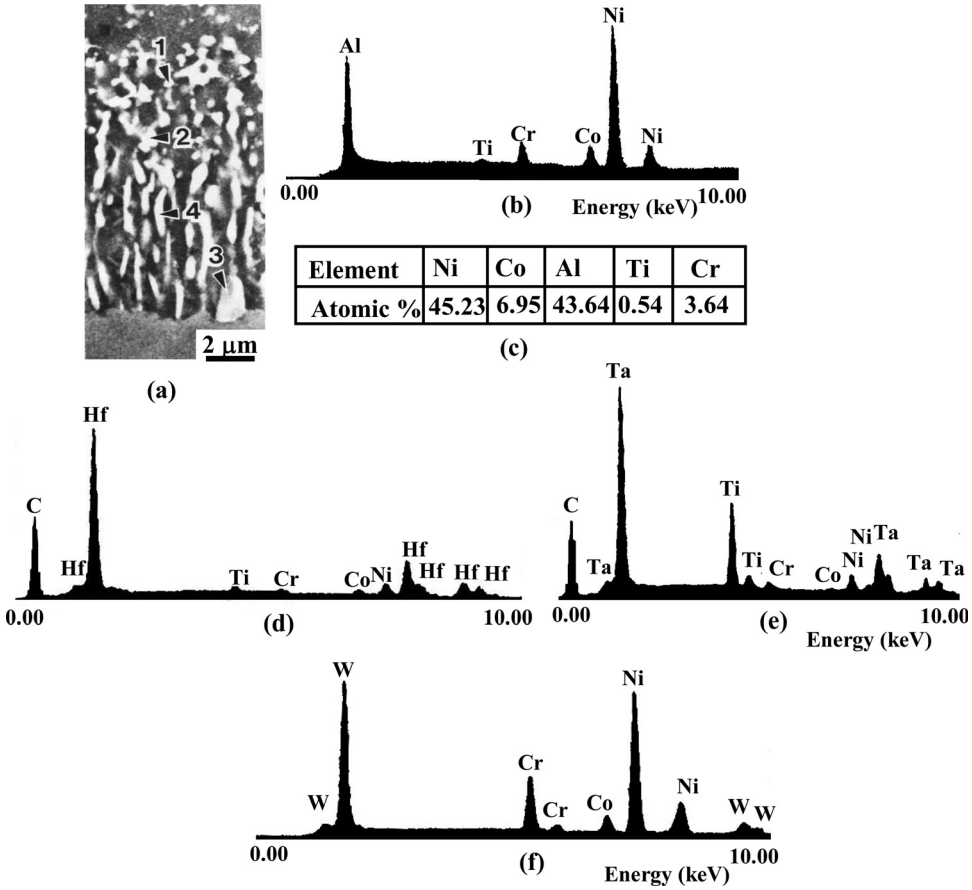

Fig. 4 Analysis of the composition of interdiffusion zone of the coating on alloy MAR M 002DS in the as-deposited condition. (*a*) Backscattered SEM composition image showing the microstructure of the interdiffusion zone. (*b*) Energy dispersive X-spectrum illustrating the elemental composition of the matrix phase (region marked 1). (*c*) Composition of the matrix phase as determined by electron probe microanalysis. (*d*), (*e*), and (*f*) are energy dispersive X-spectra illustrating the elemental compositions of the precipitates marked 2, 3, and 4, respectively, in (*a*).

demonstrated in Figs. 4(*d*) and 4(*e*) in addition to the Ni–Cr–W σ-phase (Fig. 4(*f*)).

3.2 Comparative Coating Performance: Thermal Stability Characteristics and Oxidation Behavior. Figure 5 shows comparative performance of the coating system on alloys CMSX-4 and MAR M 002DS as determined from thermal exposure tests at 1150 °C with a 24-h cycling period to room temperature. Failure was indicated by macroscopic spallation of the top coat. It is observed that the coating on alloy MAR M 002DS outperformed that on the alloy CMSX-4, which could be explained in terms of differences in thermal stability characteristics and oxidation behavior as shown below.

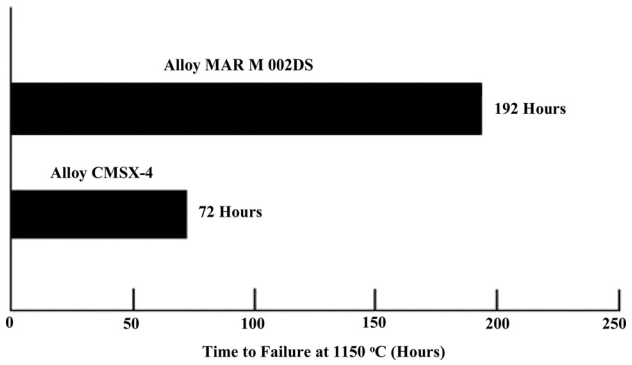

Fig. 5 Comparative performance of the coating system on alloys CMSX-4 and MAR M 002DS as determined from thermal exposure tests at 1150 °C in air with a 24-h cycling period to room temperature

As an example, Figs. 6(*a*) and 6(*b*) illustrate the effect of 48 h of exposure at 1150 °C with a 24-h cycling period to room temperature on the microstructures along a cross-section of the bond and into the substrate. In case of alloy CMSX-4 (Fig. 6(*a*)), a considerable growth of the interdiffusion zone was observed. Also, the β-phase in the outermost coating layer was partially transformed into the γ'-phase. However, in the case of alloy MAR M 002DS (Fig. 6(*b*)), the microstructure remained qualitatively similar to that in the as-deposited condition (Fig. 1(*b*)), although the thickness of the outermost layer containing $PtAl_2$ and β-phase was reduced. The presence of the γ'-phase in the outermost coating layer of alloy CMSX-4 is demonstrated in the results of TEM experiments shown in Figs. 6(*c*)–6(*e*). In <111> orientation, the β-phase in the bright-field TEM image of Fig. 6(*c*) is distinguished from the γ'-phase by the characteristic superlattice reflections. In the case of the β-phase, the diffraction pattern resembles that of a disordered body-centered cubic crystal (Fig. 6(*d*)), however, in the case of the γ'-phase, superlattice reflections appear at every 1/2-position of the fundamental reflection.

The tendency of the β-phase to transform into the γ'-phase could be related to outward diffusion of Ni as well as other substrate elements. Simultaneously, the Pt content in the outermost layer was reduced due to inward diffusion of Pt. These processes

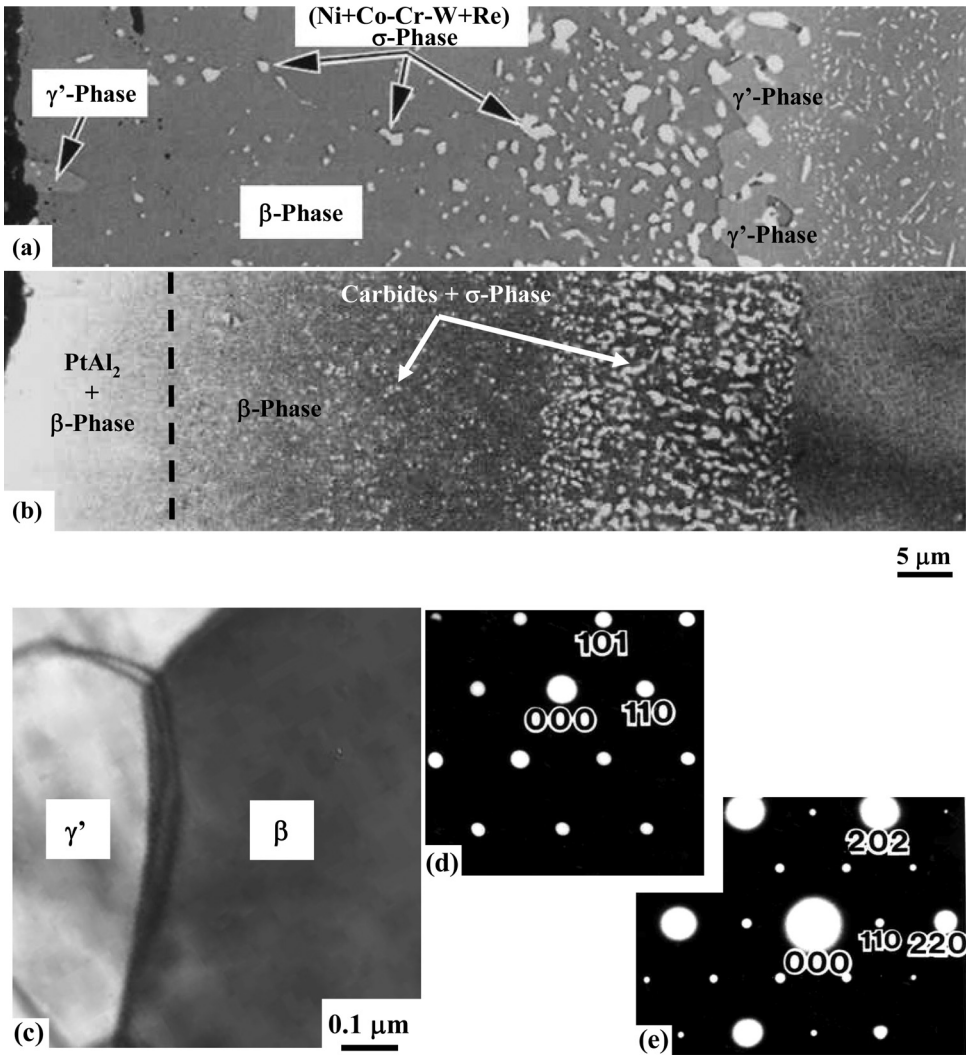

Fig. 6 Examples illustrating comparative thermal stability characteristics of the bond coat during thermal exposure at 1150 °C. (*a*) and (*b*) are backscattered SEM composition images illustrating the effect of 48 h of exposure at 1150 °C on the microstructure of the bond coat on alloys CMSX-4 and MAR M 002DS, respectively. (c) Bright-field TEM image showing the presence of γ'-phase in the outermost coating layer on alloy CMSX-4. (*d*) and (*e*) are characteristic diffraction patterns of γ'-phase and β-phase in <111> orientation, respectively.

were found to occur more rapidly in the case of alloy CMSX-4, which could be related to lower stability of its interdiffusion zone as described. This is further illustrated in Fig. 7 showing comparative kinetics of interdiffusion for the two alloys expressed as fractional growth of the interdiffusion zone per unit time. As can be seen, the kinetics of interdiffusion followed a nearly parabolic rate behavior and the activation energy was about the same for both alloys (290 kJ/mol) suggesting that interdiffusion occurred by the same mechanism for both alloys. However, interdiffusion occurred at a faster rate in the case of alloy CMSX-4 consistent with the expected lower stability of its interdiffusion zone. Since diffusion data for intermetallic compounds is rather scarce, it was difficult to correlate the estimated activation energy with a particular diffusion mechanism. As expected, direct correlation was found to exist between the thermal stability characteristics and oxidation behavior as demonstrated by the results presented below.

Because of the lower thermal stability of the bond coat on alloy CMSX-4 as demonstrated above, less protective oxides would be expected to form during the earlier stages of thermal exposure at a given temperature in comparison with the case of alloy MAR M 002DS. This is consistent with the coating life data shown in Fig. 5 and further confirmed by the observed growth rates of the thermally grown oxide as described below.

Figure 8(*a*) shows the effect of exposure time at 1150 °C on the thickness of the thermally grown oxide (total oxide thickness - thickness of initial oxide layer present in the as-deposited condition). Although the stage of primary oxidation was followed by a steady state for both alloys, breakaway oxidation occurred earlier in the case of alloy CMSX-4. This suggested that coating failure occurred by the same mechanism in both alloys; however, the corresponding kinetics were accelerated in the case of alloy CMSX-4. As an example, Figs. 8(*b*) and 8(*c*) show the microstructure of the Al_2O_3 oxide layer developed by the bond coat on alloys CMSX-4 and MAR M 002DS, respectively, after 48 h of exposure at 1150 °C. It is observed that alloy MAR M 002DS (Fig. 8(*c*)) differed from alloy CMSX-4 (Fig. 8(*b*)) in that the oxide layer contained Hf-rich oxide pegs extending into the bond coat and enveloped by Al_2O_3, which is typical behavior of reactive elements such as Hf, e.g., Ref. [10]. This is well known to improve the adhesion of the oxide scale.

Based upon the above observations, it could be concluded that the variation in coating performance on alloys CMSX-4 and MAR M 002DS could be related to differences in their chemical compositions influencing both the thermal stability characteristics and oxidation behavior of the bond coat. Although loss of loss of adhesion between the thermally grown oxide and bond coat was the

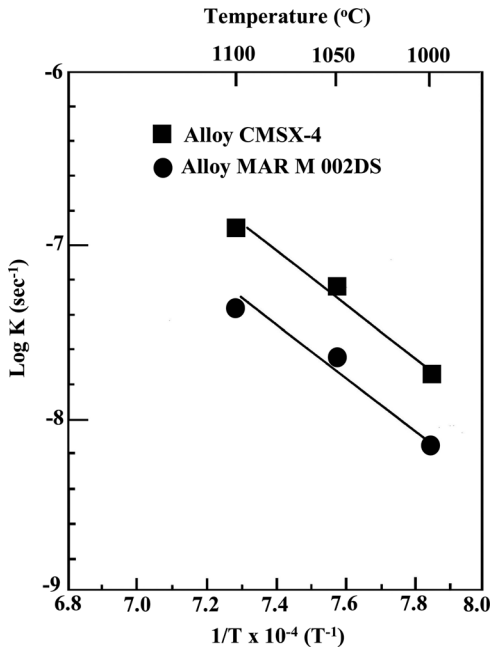

Fig. 7 Temperature dependence of the parabolic rate constant (*K*) of interdiffusion between the bond coat and the superalloy substrates

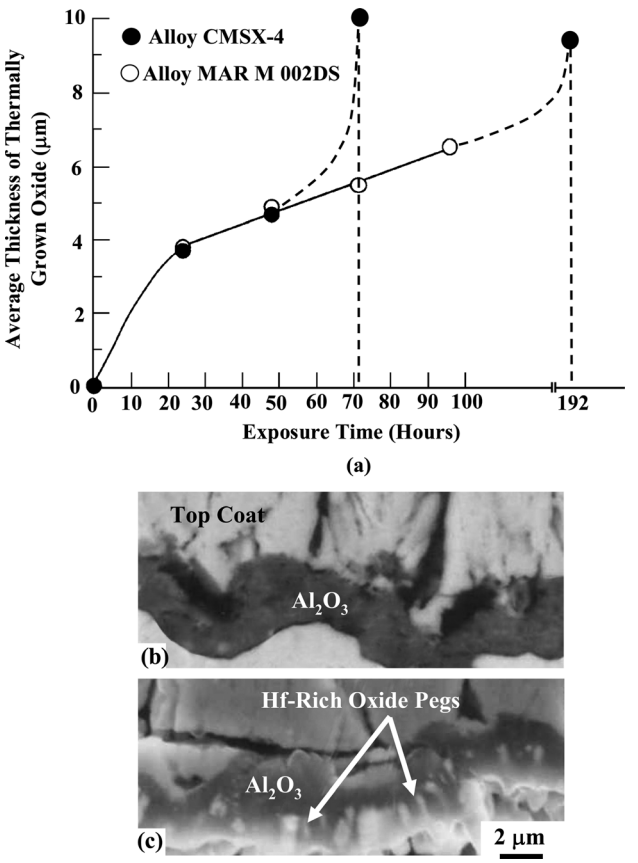

Fig. 8 Comparative oxidation behavior of the bond coat during thermal exposure at 1150 °C. (*a*) Thickening rate of the thermally grown oxide. (*b*) and (*c*) are backscattered SEM composition image showing the microstructures of the thermally grown oxide corresponding to alloys CMSX-4 and MAR M 002DS, respectively, after 48 h of exposure.

mode of failure for both alloys, the underlying mechanism was different as shown below.

3.3 Comparative Failure Mechanism of the Coating System. For both alloys, the surface of the ceramic top coat exposed by the failure was covered by the thermally grown oxide indicating that the mode of failure was loss of adhesion between the oxide and bond coat. In the case of alloy CMSX-4, oxide particles enriched in Ta and Ti were observed beneath the thermally grown layer of Al_2O_3. For alloy MAR M 002DS, the presence of Hf-rich oxide was more pronounced. However, the mechanisms leading to spallation of the thermally grown oxide could be identified from examination of the bond coat surface exposed by the failure as demonstrated in Fig. 9.

Due to the nature of the mechanism leading to oxide spallation, secondary SEM imaging in the case of alloy CMSX-4 was more revealing. Characteristically, the bond coat surface contained high density of voids as shown in the example of Fig. 9(*a*). At higher magnifications oxide particles enriched in Ta and Ti could be detected in some voids. Depending upon their concentrations, Ti and Ta could degrade the adherence of Al_2O_3 by forming Ta and Ti-rich oxide particles near the oxide-metal interface [11–13]. This can lead to oxide decohesion by coalescence of voids formed around the oxide particles. However, it is also possible that the formation of less protective oxides due to interdiffusion with the superalloy substrate could significantly contribute to the observed accelerated oxidation toward the end of the coating life (Fig. 8(*a*)).

In the case of alloy MAR M002DS, backscattered composition SEM imaging was more revealing in studying the characteristics of the bond coat surface exposed by the failure. Unlike the case of alloy CMSX-4, the bond coat surface contained islands of Al_2O_3 containing particles of Hf-rich oxide as shown in the backscattered image of Fig. 9(*c*) and corresponding energy dispersive X-spectra of Figs. 9(*d*) and 9(*e*). This observation suggested that fracture of the Hf-rich oxide pegs near the oxide-bond coat interface observed in Fig. 8(*c*) had played an important role in the loss of adhesion between the thermally grown oxide and bond coat. Usually, this behavior is encountered in Al_2O_3-forming alloy systems containing reactive elements because of the nature of the distribution of growth stress in the vicinity of the oxide pegs [10,13,14]. To summarize, the schematics of Fig. 10 illustrate the sequence of events, which could lead to loss of adhesion between the thermally grown oxide and bond coat on both alloys as depicted from experimental observations. A better understanding of the factors governing the adhesion of the thermally grown oxide and in turn, the useful life of the coating can be developed by considering the influence of key elements in the superalloy substrate as well as in the bond coat as described below.

It was shown that minor amounts of sulfur in the superalloy substrate can degrade the adherence of the oxide scale because of its tendency to segregate at the surface, which could lead to forming voids at the oxide-metal interface and/or weakening of the oxide-metal bond [15]. However, the presence of Pt in aluminide coating was found to eliminate or minimize the detrimental effect of sulfur [15,16]. Other beneficial effects of Pt include purer oxide scale of slower growth rate as well as increasing the diffusional stability of the bond coat [15–18]. Consistent with these results, it is also found that Pt promotes selective oxidation of Al by suppressing the formation of nonprotective oxides particularly NiO in the case the Pt+Hf-modified γ'-γ bond coats [19]. Reactive elements such as Hf and Y are well known to improve the protective nature of Al_2O_3 particularly its adherence to the underlying substrate, e.g., Refs. [15,16,19–22]. It is interesting to note that some common beneficial effects of Hf and Y have been reported particularly their effects on the grain morphology of Al_2O_3 scale. Both Hf [15,16,19,20], and Y [21,22] were observed to promote the formation of columnar grains of

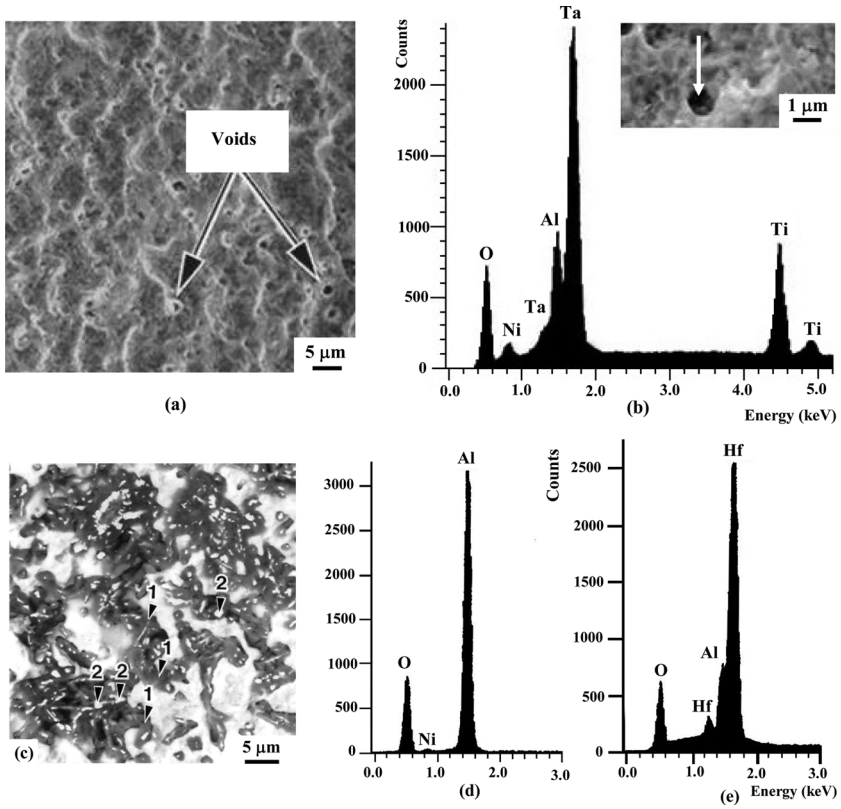

Fig. 9 Microstructural features of the bond coat surface exposed by failure of the coating system on alloys CMSX-4 (*a*), (*b*) and MAR M 002DS (*c*), (*d*), and (*e*) during thermal exposure at 1150 °C with a 24-h cycling period to room temperature. (*a*) Secondary SEM image showing the microstructure of the bond coat surface exposed by failure of the coating system on alloy CMSX-4 after 72 h of exposure. (*b*) Corresponding secondary SEM image at higher magnification and energy dispersive spectrum showing the presence of Ta,Ti-rich oxide particles within voids at the coating surface. (*c*) Backscattered SEM composition image showing the microstructure of the bond coat surface exposed by failure of the coating system on alloy MAR M 002DS after 192 h of exposure. (*d*) and (*e*) are corresponding energy dispersive X-spectra showing the elemental compositions of regions *a* and 2 in (*c*).

Al_2O_3 improving their fracture toughness. However, because higher concentrations of reactive elements can produce undesirable effects and in the meantime Pt is found to combat some of these effects, it is important that Pt-modified bond coats contain balanced amounts of Pt and reactive elements to achieve optimum oxidation resistance [20].

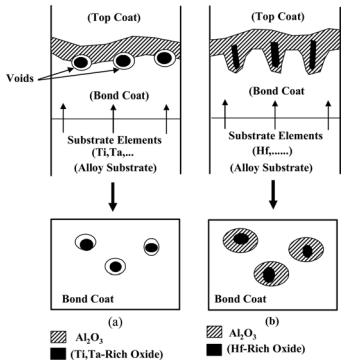

Fig. 10 Schematics illustrating possible mechanisms leading to decohesion between the thermally grown oxide and underlying bond coat. (*a*) Alloy CMSX-4: coalescence of voids formed around Ta,Ti-rich oxide particles near the oxide-bond coat interface. (*b*) Alloy MAR M 002DS: fracture of Hf-rich oxide pegs.

4 Conclusion

Experiment showed that the Pt-aluminide bond coat in a thermal barrier coating system on alloy MAR M 002DS outperformed that on alloy CMSX-4 because of differences in chemical compositions of the two alloys influencing the structure of the interdiffusion zone in the as-deposited condition as well as the thermal stability characteristics and oxidation behavior of the bond during thermal exposure at elevated temperatures. Although for both alloys, the mode failure was loss of adhesion between the thermally grown oxide and bond coat, the underlying mechanism was different. In the case of alloy CMSX-4, oxide decohesion occurred by void formation around Ta, Ti-rich oxide particles neat the oxide-bond coat interface and their subsequent coalescence. However, in the case of alloy MAR M 002DS, oxide decohesion was facilitated by fracture of Hf-rich oxide pegs enveloped by Al2O3 near the oxide-bond coat interface.

Acknowledgment

It is a pleasure to acknowledge the continued support of King Fahd University of Petroleum & Minerals as well as the Saudi Ministry of Higher Education.

References

[1] Pomeroy, M. J., 2005, "Coatings for Gas Turbine Materials and Long Term Stability Issues," Mater. Des., **26**(3), pp. 223–231.

[2] Evans, A. G., Mumm, D. R., Hutchinson, J. W., Meier, G. H., and Petit, F. S., 2001, "Mechanisms Controlling the Durability of Thermal Barrier Coatings," Prog. Mater. Sci., **46**, pp. 505–553.
[3] Tawancy, H. M., and Al-Hadhrami, Luai M., 2011, "Influence of Titanium in Nickel-Base Superalloys on the Performance of Thermal Barrier Coatings Utilizing γ-γ' Platinum Bond Coats," J. Eng. Gas Turbines Power, **133**(4), p. 042101.
[4] Lammermann, H., and Kienel, G., 1991, "PVD Coatings for Aircraft Turbine Blades," Adv. Mater. Processes, **140**(6), pp. 18–23.
[5] Hayashi, S., Ford, S. I., Young, D. J., Sordelet, D. J., Besser, M. F., and Gleeson, B., 2005, "α-NiPt(Al) and Phase Equilibria in the Ni-Al-Pt System at 1150°C," Acta Mater. **53**(11), pp. 3319–3328.
[6] Tomaszewicz, P., and Wallwork, G. R., 1982, "The Degradation of Alumina-Forming Coating System on Nickel, Cobalt and Iron-Based Alloys by High Temperature Oxidation," *Reviews of High Temperature Materials*, J. Newkirk, ed., Freund Publishing House, London, pp. 51–60.
[7] Hoppin, G. S., and Danesi, W. P., 1987, "Future of Superalloys" *Superalloys II*, C. T. Sims, N. S. Stoloff, and W. C. Hagel, eds., Wiley, New York, pp. 552–553.
[8] Wallwork, G., and Croll, J., 1976, "A Review of the Strengthening Mechanisms in Iron and Nickel Based Fe-Ni-Cr Alloys Used at High Temperatures" *Reviews of High Temperature Materials*, J. Newkirk, ed., Freund Publishing House, London, pp. 117–125.
[9] Anton, D. L., Shah, D. M., Duhl, D. N., and Giamei, A. F., 1989, "Selecting High-Temperature Structural Intermetallic Compounds: The Engineering Approach," J. Met., **41**(6), pp. 12–17.
[10] Stott, F. H., 1989, *The Role of Active Elements in the Oxidation Behavior of High Temperature Metals and Alloys*, E. Lang, ed., Elsevier Applied Science, London), pp. 3–22.
[11] Smialek, J. L., and Meier, G. H., 1987, *Superalloys II*, C. T. Sims, N. S. Stoloff, and W. C. Hagel, eds., Wiley, New York, pp. 293–326.
[12] Levy, M., Farrell, P., and Pettit, F., 1986, "Oxidation of Some Advanced Single-Crystal Nickel- Base Superalloys in Air at (2000) F (1093°C)," Corrosion-NACE, **42**(12), pp. 708–717.
[13] Jedlinski, J., 1992, "The Influence of Reactive Elements on the High Temperature Oxidation Behavior of Alumina-Forming Materials," Solid State Phenom., **21 & 22**, pp. 335–390.
[14] Nicholls, J. R., and Hancock, P., 1989, *The Role of Active Elements in the Oxidation Behavior of High Temperature Metals and Alloys*, E. Lang, ed., Elsevier, London, pp. 195–224.
[15] Haynes, J. A., Pint, B. A., More, K. L., Zhang, Y., and Wright, I. G., 2002, "Influence of Sulfur, Platinum, and Hafnium on the Oxidation Behavior of CVD NiAl Bond Coatings," Ox. Met., **58**(5/6), pp. 513–544.
[16] Wright, I. G., and Pint, B. A., 2005, "Bond Coat Performance of Thermal Barrier Coatings for Industrial Gas Turbines," Proc. IMechE, Part A: J. Power Energy, **219**, pp. 1–10.
[17] Tawancy, H. M., and Al-Hadhrami, L.M., 2010, "Role of Platinum in Thermal Barrier Coatings Used in Gas Turbine Blade Applications," J. Eng. Gas Turbine Power, **132**(2), p. 022103.
[18] Tawancy, H. M., Abbas, N. M., and Rhys-Jones, T.N., 1991, "Role of Platinum in Aluminide Coatings," Surf. Coatings Technol., **49**(1–3), pp. 1–7.
[19] Mu, N., Izumi, T., Zhang, L., and Glesson, B., 2008, "The Development and Performance of Pt+Hf -Modified γ'-Ni3Al+γ-Ni Bond Coatings for Advanced Thermal Barrier Coating Systems," *Superalloys 2008*, R. C. Reed et al., eds. The Minerals, Metals, and Materials Society, pp. 629–637.
[20] Haynes, J. A., Ferber, M. K., Porter, W. D., and Rigney, E. D., 1999, "Characterization of Alumina Scales Formed During Isothermal and Cyclic Oxidation of Plasma-Sprayed TBC Systems at 1150°C," Ox. Met., **52**(1/2), pp. 31–76.
[21] Tawancy, H. M., and Sridhar, N., 1992, "High-Temperature Oxidation Behavior of a Ni-Cr-Al-Fe-Y Alloy," Ox. Met., **37**(3–4), pp. 143–166.
[22] Tawancy, H. M., 1991, "On the Role of Y During High-Temperature Oxidation of a Ni-Cr-Al-Fe-Y Alloy," Metall. Trans. A, **22**(6), pp. 1463–1465.